



Three-dimensional porous hollow microspheres of activated carbon for high-performance electrical double-layer capacitors



Lu Wei^{*1}, Kuan Tian¹, Yiyi Jin, Xingyan Zhang, Xin Guo^{**}

Laboratory of Solid State Ionics, School of Materials Science and Engineering, Huazhong University of Science and Technology, Wuhan, 430074, PR China

ARTICLE INFO

Article history:

Received 29 December 2015

Received in revised form

8 March 2016

Accepted 10 March 2016

Available online 12 March 2016

Keywords:

Activated carbon

Microspheres

Porous hollow structure

Bio-template

Electrical double-layer capacitors

ABSTRACT

As energy storage and delivery devices, electrical double-layer capacitors (EDLCs) with nanostructured activated carbon electrodes from natural organic precursors have attracted considerable attention, particularly for high-performance commercial EDLCs. Conventional methods for synthesizing activated carbons offer limited control on their morphology and structure. In this work, microspheres of activated carbon were synthesized by employing lotus pollens as both the carbon source and self-template combined with CO₂ activation. The prepared activated carbon microspheres (ACMs) own porous (pore size mainly in 1–3 nm) hollow structure with three-dimensional nanorod network constructed shell. EDLCs with the unique ACMs as electrodes showed high specific capacitance (244 F g⁻¹ at 0.1 A g⁻¹ in 1 M H₂SO₄ electrolyte), superior rate capability (83% retention at 20 A g⁻¹), remarkable frequency response and excellent charge–discharge cycling stability (no capacitance fading during 10,000 charge–discharge cycles). The ACMs are very attractive as electrode material for high-performance EDLC applications.

© 2016 Elsevier Inc. All rights reserved.

1. Introduction

Electrical-double layer capacitors (EDLCs), as one type of supercapacitors, store the charge electrostatically by charging the electrochemical double-layer. The charge separation occurs through polarization at the electrode-electrolyte interface by using electrochemically stable and high specific surface area (SSA) materials as electrodes [1]. Owing to the charge storage mechanism, EDLCs offer a high power delivery or uptake, sub-second charging and ultra-long cycle life, which make them attractive for a wide range of applications, including consumer electronics, memory back-up systems, uninterruptable power supplies, smart grid systems, hybrid electric vehicles (HEVs), load-leveling applications and so on. The demanding applications require further increase in the energy density of EDLC technology, decrease in cost and enhancement in safety, at the same time maintaining their high power capacity [2,3].

The energy density of an EDLC is proportional to the specific capacitance and operational voltage according to the energy

equation ($E = 1/2 CV^2$). Since the operational voltage is determined by the electrolyte used in real applications, the specific capacitance of EDLCs plays a vital role in achieving high energy density. The key to reach high specific capacitance by charging the double-layer capacitors is to use high SSA and electronically conducting electrode materials with an optimized porosity [4].

Carbon-based active materials with high surface area, high electrical conductivity, good electrochemical stability and open porosity satisfy all the requirements for EDLCs and have been extensively studied, including activated carbons, templated carbons, carbide-derived carbons, carbon fabrics/fibers, carbon nanotubes, carbon onions, carbon aerogel, graphene and graphene-based materials [5]. Among them, activated carbons [6,7] due to their high SSA, relatively low cost, great cycle stability, well-developed manufacturing technologies and easy production in large quantities have been the most widely used electrode materials in commercial EDLCs today. Templated carbons [8,9] and carbide-derived carbons [10–12] offer tight pore size control and high surface area, but their preparation processes need to use toxic chemicals (such as high corrosive HF acid and Cl₂ gas) to etch templates or remove metal from carbides, and employ multi-step purification procedures. Hence these technologies are difficult to achieve the mass production required for the EDLC manufactures. Carbon fabrics/fibers [13] after activation can reach the same

^{*} Corresponding author.

^{**} Corresponding author.

E-mail addresses: lwei@hust.edu.cn (L. Wei), xguo@hust.edu.cn (X. Guo).

¹ The authors contribute equally to this work.

capacitance as activated carbon powders, since they have similar SSA, but the high price limits their use to specialty applications. Carbon nanotubes [14–16], carbon onions [17,18] and carbon aerogels [19,20] with large mesopores and macropores commonly offer high rate property, but relatively low gravimetric and volumetric specific capacitances. Graphene [21–25] possessing a high theoretical surface area ($2630 \text{ m}^2 \text{ g}^{-1}$) and superior electrical conductivity, however, due to the unavoidable aggregation of graphene nanosheets during processing, the real surface area of graphene is far below the theoretical one. In addition, due to its very high pore volume and thus low density, graphene electrodes commonly offer limited gravimetric capacitance and especially volumetric capacitance. Activation of graphene [26,27] can improve its performance but still not yet match the performances of the most advanced activated, template and carbide-derived carbons. Therefore, activated carbons will remain the material choice and keep dominating the EDLC market in the near future. By choosing appropriate carbon sources, developing novel synthesis methods and well-controlling the structure and porosity properties of activated carbon materials are of demands for the further development of commercial EDLC technology.

Activated carbons are derived from carbon-rich precursors by high-temperature pyrolysis (carbonization) in an inert atmosphere with subsequent selective oxidation by chemical (such as in KOH, H_3PO_4 or ZnCl_2) or physical (such as in CO_2 or water vapor) activation to increase the SSA and pore volume [6]. Petroleum coke, pitch and coal used to be the most common carbon sources for activated carbon productions. Considering the global growing energy consumption and environmental issues caused by fossil fuel combustion, natural and sustainable organic precursors from agricultural and forest residues, such as coconut shell [28,29], apricot shell [30], cherry stone [31], rice husk [32], sun flower seed shell [33], banana fibers [34], potato starch [35], melaleuca barks [36], beer lees [37], corn grain [38], sugar cane bagasse [39], coffee grounds [40], wheat straw [41] and pollens [42], have been explored as carbon sources to prepare activated carbons for supercapacitors. However, all of these precursors were carbonized and activated *via* chemical activation (in KOH, NaOH or ZnCl_2), resulting in relatively high SSA and large mesopores, which is in favor of getting good rate performance. In addition, after the activation step, the activated carbons present almost the morphology and structure of irregular shaped fragments, subsequent ball milling or grinding to lower the particle size is normally necessary. Compared with chemical activation, physical activation using CO_2 or steam as activation agent, does not need post-processing to remove metal ions in the activated carbons introduced by activation agents, thus it does not lead into impurities, and is a low cost, simple and environmentally friendly process. More importantly, physical activation does not change the original morphology and structure of carbon targets. It contributes to maintain the featured morphology as one expected, and at the same time, increases the SSA and pore volume of the carbon targets [43].

In this work, we utilized biological resource, lotus pollens, as carbon precursors, which are abundant, regenerative and inexpensive. Lotus pollens possess a kind of mono-dispersed microspherical structure with life-related substances in the core and distinctive micro/nano architecture on the shell. By employing lotus pollens as both the carbon source and self-template, hollow activated carbon microspheres with three-dimensional (3D) porous shell were fabricated; the morphology and structure of lotus pollens were almost ideally preserved. To the best of our knowledge, up to now there are only two works [42,44] related to pollen-derived materials as electrode for supercapacitors. Zhang et al. [42] used various pollens as carbon sources to produce activated carbon for EDLCs. However, after hydrothermal carbonization and

chemical activation (KOH) treatment, they just got solid irregular shaped activated carbon particles, which showed the highest capacitance of 207 F g^{-1} in EMIMBF₄ electrolyte. Very recently, Li et al. [44] synthesized hollow MnO_2/C composite by utilizing lotus pollens as template. But without high-temperature carbonation and activation, the MnO_2/C composite possesses relatively low electrical conductivity and specific surface area. With the contribution of pseudocapacitance induced by MnO_2 nanosheets, supercapacitors with the MnO_2/C electrodes showed specific capacitance of 257 F g^{-1} in 1 M Na_2SO_4 electrolyte, yet lower rate capability and cycle stability than those of EDLCs with activated carbons electrodes. We are confident that the porous hollow microspheres of activated carbon would provide an ideal model of electrode materials for EDLCs to investigate the relationship between the special porous structure and the electrochemical performances.

2. Experimental

2.1. Preparation of activated carbon microspheres

2.1.1. Pre-treatment of lotus pollens

Firstly, the purchased lotus pollens (10 g) were immersed into acetone solution (70 ml) with ultrasonic treatment for 2 h. Next, they were filtered and washed with ethanol and deionized water, then dried in an oven at 70°C for 12 h. The above process could clean impurities on the exine and remove the core substances in pollen grains, such as proteins, amino acids, vitamins and nucleic acids. Afterward, the cleaned lotus pollens were heated in an oven at 300°C in air for 6 h. This process could fix the morphology of lotus pollens, and avoid the structural collapse in the following high-temperature heat-treatment.

2.1.2. Carbonization and activation of pre-treated lotus pollens

After calcination at 300°C in air, the pre-treated lotus pollens were transferred into a tube furnace and heated to 700°C at a heating rate of $10^\circ\text{C min}^{-1}$ in Ar gas (250 ml min^{-1}) for 2 h. After cooling to room temperature, carbonized black powders were obtained. The powders were subsequently heated to 900°C at a heating rate of $10^\circ\text{C min}^{-1}$ in an Ar flow (250 ml min^{-1}) and then activated using a pure CO_2 gas (150 ml min^{-1}) for 2–6 h. After activation, the samples were cooled down in Ar to minimize the possible formation of surface groups at elevated temperatures. These activated carbon samples are tagged as ACM-2h, ACM-4h and ACM-6h with reference to different activation hours.

2.2. Characterization of activated carbon microspheres

The morphology of the prepared activated carbon microspheres was observed by a Sirion 200 (FEI Corporation, Netherlands) field emission scanning electron microscope (FE-SEM). The surface and pore characterization of activated carbon microspheres were characterized by N_2 adsorption/desorption measurements at -196°C using an ASAP 2020 surface area and porosity analyzer (Micromeritics Instrument Corporation, USA). Before analyzing, the activated carbon microspheres were degassed at 300°C using the VacPrep 061 degasser (Micromeritics Instrument Corporation, USA) to remove moisture and adsorbed contaminants. The SSA of activated carbon microspheres are calculated from N_2 adsorption isotherms using the Brunauer–Emmett–Teller (BET) equation in the range of relative pressures from 0.1 to 0.3. Porosity distributions were calculated by the nonlocal density functional theory (NLDFT) analysis of N_2 adsorption in carbon slit pores. Raman spectra were recorded using LabRAM HR800 spectrometer (HORIBA Jobin Yvon Corporation, France). The source of radiation was a Nd:YAG laser

operating at a wavelength of 532 nm and a power of 50 mW. X-ray photoelectron spectroscopy (XPS) analyses were performed on an AXIS Ultra DLD-600 W spectrometer (Kratos Corporation, Japan) with a monochromatic Al K α X-ray source.

2.3. Fabrication of EDLCs and electrochemical measurements

Electrodes were made by mixing 90 wt. % activated carbon microspheres and 10 wt. % polytetrafluoroethylene (PTFE) in ethanol on a hotplate. After stirring uniformly and evaporating redundant ethanol, composite of activated carbon microspheres–PTFE was formed. The produced composite was then rolled into ~150 μm thick sheet and cut into the size of 1 cm \times 1 cm for EDLC electrodes. Before assembling EDLCs, the electrodes were placed into a vacuum oven (120 $^{\circ}\text{C}$) overnight to remove the moisture and residual hydrocarbons. After cooling to room temperature, they were taken out from the vacuum oven for weighing immediately. Sandwich-type electrochemical cell was set up with two symmetrical electrodes separated by a polyethylene separator with hydrophilic modification (average pore size of 0.4 μm , porosity of 60% and 0.14 mm in thickness). Gold foil was attached to each electrode and served as current collector because of its high corrosion resistance and stability. Then the sandwich-type cell was clamped by two PTFE sheets (3 mm in thickness) and immersed in 1 M H_2SO_4 electrolyte in a glass beaker. The glass beaker was covered with Parafilm. 1 M H_2SO_4 solution was used as electrolyte, because of its high conductivity, low internal resistance, and smaller ionic radius compared with organic or ionic liquid electrolytes. Moreover, aqueous 1 M H_2SO_4 has mobile H^+ ions, which gives enhanced access to micropores, thus favors to study the micropore properties of the activated carbon microspheres during the electrochemical process.

All the electrochemical tests were carried out at room temperature. Cyclic voltammetry (CV) measurements were performed using a CHI660E electrochemical workstation (CH Instruments, Inc., China) in the voltage range -600 to $+600$ mV at scan rates of 1–500 mV s^{-1} . The carbon specific capacitance, C (F g^{-1}), was calculated according to the following equation:

$$C = \frac{2I}{(dV/dt)m} \quad (1)$$

where I is the current (A), dV/dt is the scan rate (V s^{-1}), and m is the mass of single carbon electrode (g). Electrochemical impedance spectroscopy (EIS) measurements were collected using a Solartron 1296 A impedance analyzer (Solartron Analytical, UK) in the frequency range of 1 mHz–100 kHz at open circuit potential with an AC amplitude of 10 mV. The carbon specific capacitance, C (F g^{-1}), was calculated according to the following equation:

$$C = \frac{2 \cdot |\text{Im}(Z)|}{2\pi f \cdot [(\text{Im}(Z))^2 + (\text{Re}(Z))^2] m} \quad (2)$$

where f is the operating frequency (Hz), $\text{Im}(Z)$ and $\text{Re}(Z)$ are the imaginary and real parts of the total device impedance (Ohm), and m is the mass of single carbon electrode (g). Galvanostatic charge–discharge tests were also measured using the CHI660E electrochemical workstation in the voltage range 0–600 mV and at current densities between 0.1 and 20 A g^{-1} . The 10,000 charge–discharge cycling test was carried out using a LANHE CT2001A charge–discharge system (Wuhan LAND Electronics Co., Ltd., China) at current load of 2 A g^{-1} . The carbon specific capacitance, C (F g^{-1}), was calculated according to the following equation:

$$C = \frac{2I}{(dV/dt)m}$$

where I is the current (A), dV/dt is the slope of the discharge curve (V s^{-1}), and m is the mass of single carbon electrode (g).

3. Results and discussion

3.1. The structure and morphology of samples

After heat-treatment (300 $^{\circ}\text{C}$ in air for 6 h and then 700 $^{\circ}\text{C}$ in Ar for 2 h), the carbonized lotus pollens perfectly retained the structure and morphology of the original pollen grains. Fig. 1 shows the SEM micrographs of the carbonized lotus pollen grains. It can be seen that the resulted carbon particles present spherical morphology (carbon microspheres) with a diameter of ~25 μm , and have a hollow structure since the core substances in the pollen grains have been removed (Fig. 1a, b). Moreover, the surface of the carbon microspheres exhibits porous interconnected vein-like structure (Fig. 1c), and the cross-section presents 3D network structure constructed by strengthening nanorods (Fig. 1d). The 300 $^{\circ}\text{C}$ heat-treatment in air is a critical step for achieving spherical carbon microspheres. Without this step, if we carbonize the pretreated lotus pollens directly at 700 $^{\circ}\text{C}$ in Ar, we could only obtain irregular carbon fragments. During the low temperature heat-treatment (300 $^{\circ}\text{C}$) in air, with the aid of oxygen, the spherical morphology of lotus pollen grains could be fixed and retained by means of cross-linking reactions of the chemical compounds in the pollens [45]. However, if the pretreated lotus pollens are heated at temperatures higher than 300 $^{\circ}\text{C}$ in air (for example 400 $^{\circ}\text{C}$), their original spherical structure would also be damaged as a result of the burning off of massive components in the pollens.

To increase the specific surface area and pore volume of the prepared carbon microspheres, CO_2 activation was performed following the 700 $^{\circ}\text{C}$ carbonization. Although the carbon microspheres were activated in CO_2 gas at 900 $^{\circ}\text{C}$ with different hours (2 h, 4 h and 6 h), they present almost the same morphology according to the SEM image analysis. The SEM Images of the typical sample ACM-6h are presented in Fig. 2. The CO_2 activation has not changed the shape and particle size of the carbon microspheres, the produced activated carbon microspheres still maintain the hollow spherical structure (Fig. 2a), even the vein-like texture of outer surface can be clearly observed as well (Fig. 2b).

Raman spectroscopy has been proven to be an essential technology for characterizing the microstructure of carbon materials [8,11,12]. Fig. 3 shows the Raman spectra of activated carbon microspheres with different activation time. We can see that all the samples show similar characteristic of highly disordered carbons. Commonly, a perfect graphite shows only one narrow G-band located at 1582 cm^{-1} , which corresponds to graphite in-plane vibrations. Disordered carbons additionally show a D-band located at ~1350 cm^{-1} , which is associated with a double-resonance Raman process in disordered carbons. The position and width of the D-band may vary, depending on the structure, uniformity and the presence of functional groups of the disordered carbons [46]. In this work, the G-bands located at ~1590 cm^{-1} slightly upshift from 1582 cm^{-1} , which is common for microporous carbons [11,47]. With prolonging activation time (from 2 h to 6 h), the relative intensities of D-bands to G-bands do not change apparently, suggesting activation duration will not affect the disorder degree of the prepared samples. The large value of the full width at half maximum (FWHM) of D- and G-bands (~120 and 60 cm^{-1}) and a high ratio of the intensities of these peaks ($I_D/I_G = 1.03$) are typical for porous carbon materials with high degree of structure disorder. Moreover,

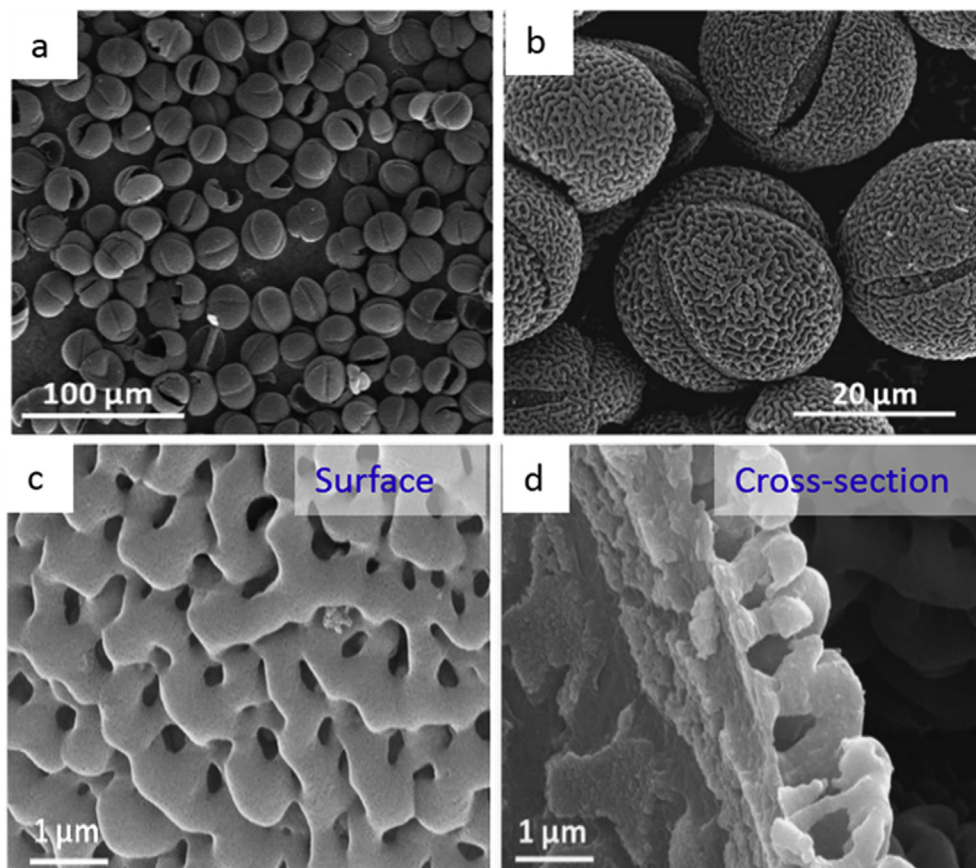


Fig. 1. (a–b) SEM images of carbonized lotus pollen grains at different magnifications and (c–d) the surface and cross-section images. Carbonization conditions: first heat-treated in air at 300 °C for 6 h and then carbonized in Ar at 700 °C for 2 h.

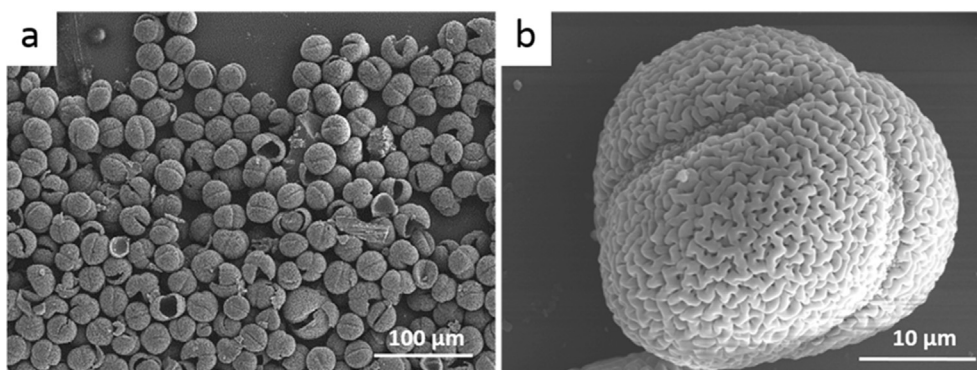


Fig. 2. (a–b) SEM images of activated carbon microspheres at different magnifications. Activation condition: heat-treatment in CO₂ at 900 °C for 6 h.

the lack of strong peaks in the spectrum range of 2400–3300 cm⁻¹ (2D, D + G, T + D, T + G, 2D' and other bands), suggests the lack of graphitic ribbon structures in these samples [48].

The XPS spectra of the activated carbon microspheres with different activation time are presented in Fig. 4. There are only two elements (C and O) detected in these samples, and the atomic fractions of oxygen are only 2–3 at. %. The O 1 s peak in Fig. 4a indicates the presence of oxygen-containing chemical bonds, which is mainly H-O-H (water molecule) in our samples. The high-resolution C 1 s spectrum for every sample (Fig. 4b) exhibits only a single strong sp² peak (C–C). The above results reveal the high purity of the activated carbon microspheres.

3.2. Surface structural properties

To study the influence of activation conditions on the development of pore structure in the activated carbon microspheres prepared from lotus pollens, the microspheres were characterized by N₂ sorption analyses at -196 °C, and the results are shown in Fig. 5. From Fig. 5a, we can see that the activated carbon microspheres with 2 h activation time (ACM-2h) exhibit classic Type I isotherm, according to the classification of the International Union of Pure and Applied Chemistry (IUPAC), which is characteristic of microporous materials. With prolonging activation time (from 2 h to 4 h, then to 6 h), the isotherms of samples ACM-4h and ACM-6h present

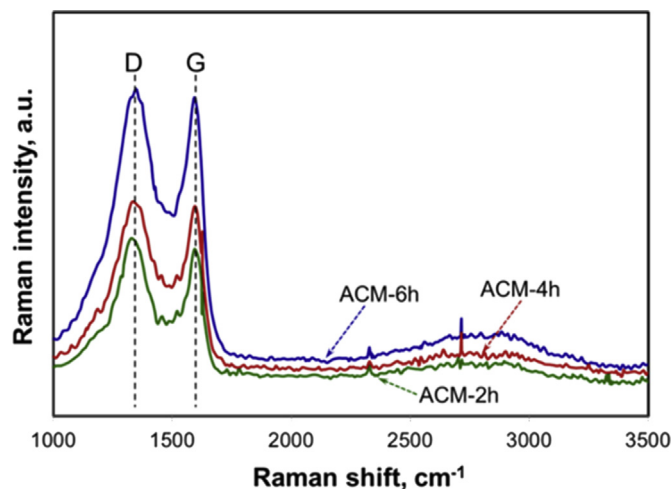


Fig. 3. Raman spectra of activated carbon microspheres with different activation hours.

continued slope above a relative pressure (P/P_0) of 0.2, suggesting the appearance of larger pores. However, the hysteresis loops in the two samples are very modest, without an obvious “knee”, which indicates that the effects of capillary condensation are not pronounced and most pores are still micropores [49]. The activation procedure significantly increased the N_2 adsorption amount along with the extending of activation time. The calculated SSA and pore

volume distribution of all the samples are summarized in Table 1. Similar to the variation of the N_2 adsorption amounts, the SSA and total pore volume (as calculated by measuring the amount of N_2 adsorbed at $P/P_0 = 0.99$) increase with the CO_2 activation time, and sample ACM-6h shows the highest SSA of $2566 \text{ m}^2 \text{ g}^{-1}$, and total pore volume up to $1.34 \text{ cm}^3 \text{ g}^{-1}$ among all the samples.

The NLDFT pore size distribution in Fig. 5b shows that the average pore size in the activated carbon microspheres is enlarged with increasing CO_2 activation time. By the further activation of micropores, including pore widening, fusing and wall collapsing, mesopores were formed. Yet, the pore size distribution is relatively narrow, mainly in the range of 1–3 nm, and mesopores appeared only when the activation time exceeds 2 h. Therefore, sample ACM-2h contains almost micropores, differently, the porosity of ACM-4h and ACM-6h is constituted mainly by micropores and a small fraction of mesopores (Table 1). The micropores are believed to be critical for achieving high capacitance values in both aqueous and organic electrolytes, due to the distortion of solvation shells and closer approach of the ions to the pore walls [10]. Yet, the appearance of mesopores is beneficial to the fast diffusion of large ions. Interestingly, our sample ACM-4h and commercial activated carbon for supercapacitors (TF-B520) have very similar porosity properties with similar SSA, pore volume and pore size distribution (Table 1).

3.3. Electrochemical performances

The specific capacitances of the EDLCs with lotus pollen-derived activated carbon microspheres as electrodes were investigated using cyclic voltammetry (CV) in 1 M H_2SO_4 aqueous electrolyte

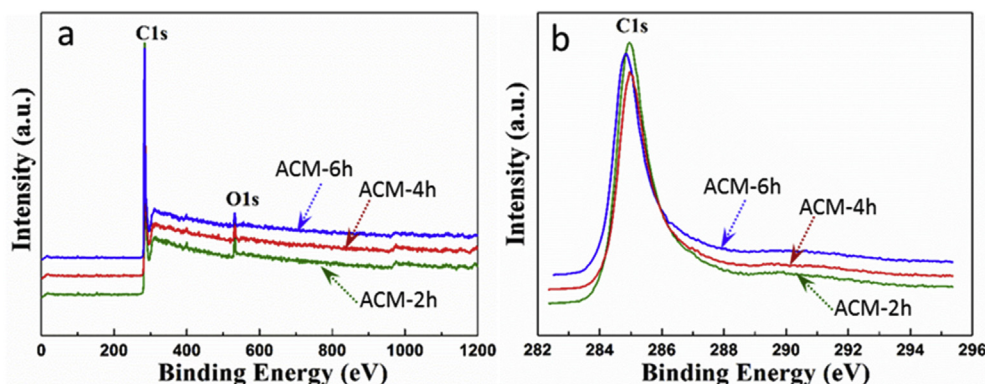


Fig. 4. (a) XPS spectra of activated carbon microspheres with different activation hours and (b) high-resolution C 1 s spectra of activated carbon microspheres.

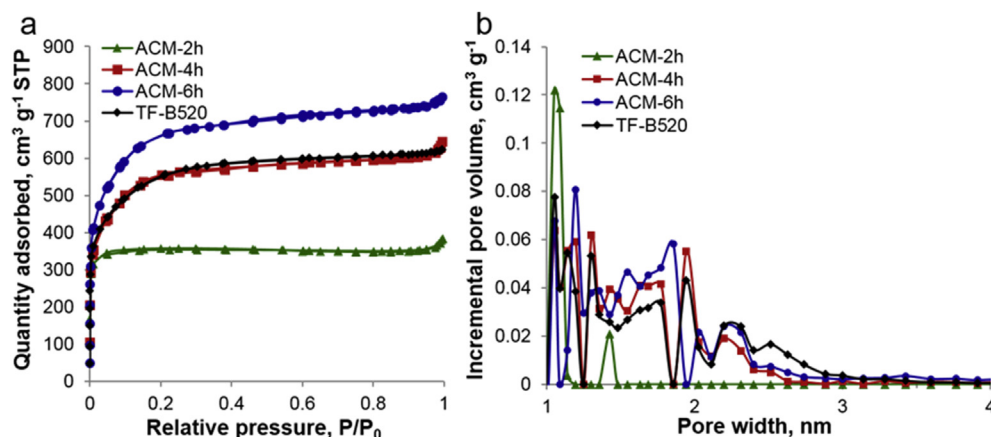


Fig. 5. (a) N_2 adsorption/desorption isotherms at -196°C and (b) pore size distribution derived from N_2 isotherms by non-local density functional theory (NLDFT) model on carbon slit pores for activated carbon microspheres and commercial activated carbon TF-B520.

Table 1

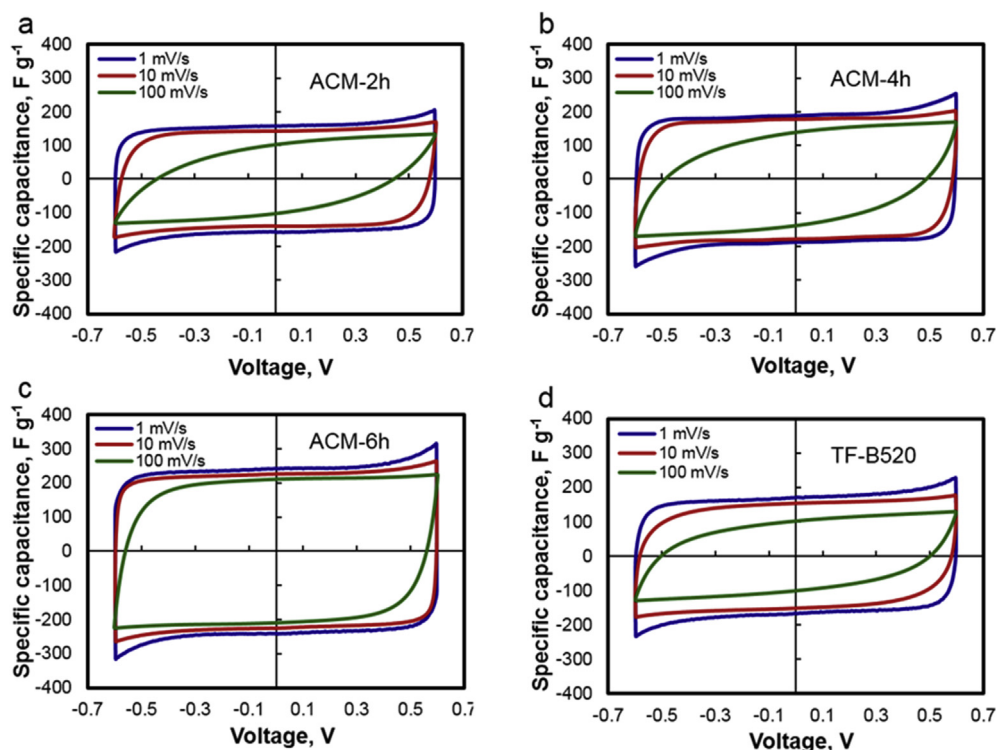
Porosity properties of the activated carbon microspheres, with commercial activated carbon TF-B520 for comparison.

Sample	BET SSA ($\text{m}^2 \text{g}^{-1}$)	Pore volume ($\text{cm}^3 \text{g}^{-1}$)	Micropore volume ($\text{cm}^3 \text{g}^{-1}$)	Mesopore volume ($\text{cm}^3 \text{g}^{-1}$)
ACM-2h	1398	0.59	0.57	0.02
ACM-4h	1962	1.00	0.77	0.23
ACM-6h	2566	1.34	0.95	0.39
TF-B520	1927	0.96	0.73	0.23

(Fig. 6a–c). At a low scan rate of 1 mV s^{-1} , all the samples show CV curves in rectangular shape with no obvious Faradaic peaks, which is the characteristic of ideal EDLCs. Among them, ACM-6h has the largest rectangular area (Fig. 6c), thus the highest specific capacitance. However, with increasing scan rates, the shapes of CV curves distort gradually for all the samples, which is common for EDLCs. When the scan rate increases to 100 mV s^{-1} , only the sample ACM-6h retains rectangular shape. The above phenomenon indicates that prolonging activation time is necessary for achieving high specific capacitance and quick ion transport into the bulk of the microspheres due to the widening of the average pore size. However, overlong activation time not only delays the preparation process, increases the production cost, but also enlarges the pore size too much, so that the SSA and specific capacitance are decreased [29,50]. The 6 h activation time is sufficient to obtain high SSA (Table 1) and desirable pore size distribution (Fig. 5b). Fig. 7a shows the specific capacitance measured at a CV scan rate of 200 mV s^{-1} as a function of pore volume. The specific capacitance was found to exhibit a good correlation with the pore volume. The increased volume of micropores and mesopores causes the SSA increase, thus leading to a higher specific capacitance. Furthermore, the sample ACM-4h has the same mesopore volume with TF-B520, but slightly higher micropore volume ($0.73 \text{ cm}^3 \text{g}^{-1}$ for TF-B520 and $0.77 \text{ cm}^3 \text{g}^{-1}$ for ACM-4h). However, even at a very high scan rate (200 mV s^{-1}), ACM-4h exhibits evidently higher specific

capacitance than TF-B520 (62 F g^{-1} for TF-B520 and 96 F g^{-1} for ACM-4h). Except for the influence of the micropore volume, the significant improved specific capacitance must be due to the unique morphology and structure of the lotus pollen-derived microspheres. Compared with the irregularly shaped structure in traditional activated carbon particles (such as TF-B520), the porous hollow microspheres with 3D nanorod network constructed shell (Fig. 1), on one hand, make the CO_2 activating agent much easier to penetrate into the micropores, widen the pore channel and eliminate the bottle-neck pores, which is critical for achieving a high specific capacitance; on the other hand, promote the electrolyte ions to diffuse into the bulk of the microspheres through the inner and outer surfaces of the spherical shells, thus making the full utilization of the entire material for charging and discharging to obtain a higher specific capacitance.

The influence of scan rates on the specific capacitances of the activated carbon microspheres and the commercial activated carbon calculated from CV measurements are summarized in Fig. 7b. Compared with samples ACM-2h, ACM-4h and TF-B520, the EDLC with ACM-6h electrodes in $1 \text{ M H}_2\text{SO}_4$ electrolyte shows the highest specific capacitance up to 235 F g^{-1} (78 F cm^{-3}), the highest capacitance retention (55%) and the best rate performance as well. Indeed, with scan rate increasing from 1 mV s^{-1} to 500 mV s^{-1} , the specific capacitance of ACM-6h gradually decreases from 235 F g^{-1} to 130 F g^{-1} , while the specific capacitance of TF-B520 decreases

**Fig. 6.** Cyclic voltammograms of (a–c) activated carbon microspheres with different activation hours and (d) commercial activated carbon TF-B520 for comparison.

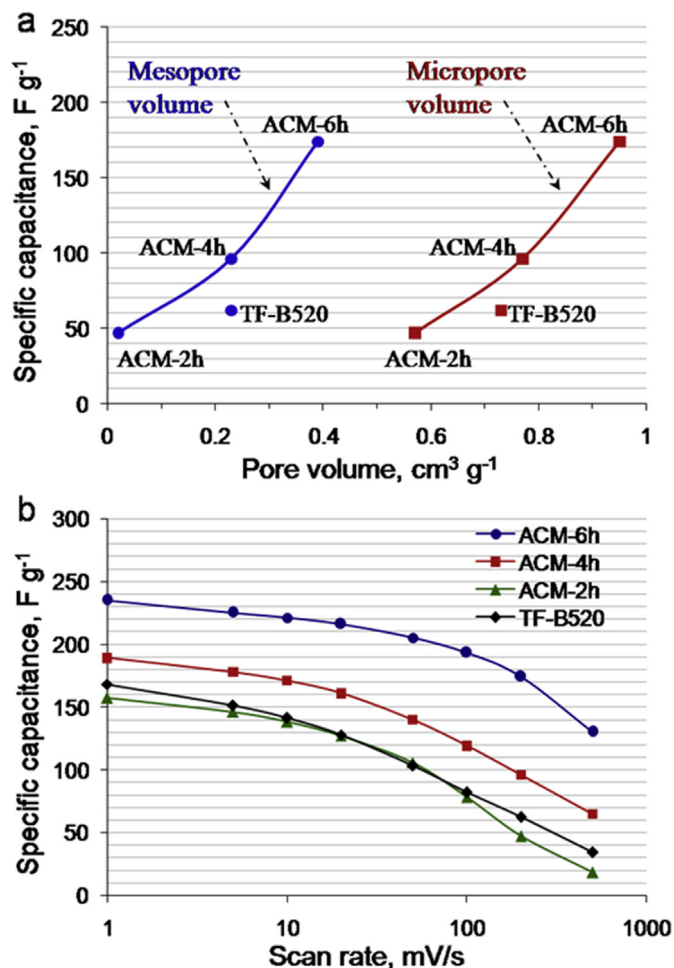


Fig. 7. (a) Specific capacitances of activated carbon microspheres at different CV scan rates, and (b) specific capacitances measured at a high scan rate of 200 mV s⁻¹ as a function of pore volume, in comparison with that of commercial activated carbon TF-B520.

from 168 F g⁻¹ to as low as 34 F g⁻¹. The fast ion transport rate and high capacitance retention make ACM-6h very attractive for the applications in high-power EDLCs.

The electrochemical impedance behaviors of the samples in 1 M H₂SO₄ electrolyte are presented in Fig. 8a. The Nyquist plots of the samples exhibit the typical features of porous electrodes with a 45° Warburg region at high-medium frequencies, and an almost vertical line at low frequencies, where the behaviors become mainly capacitive [51]. The corresponding electrical equivalent circuit is presented in the top right of Fig. 8a. At very high frequencies, the intersection of the Nyquist plot with X-axis (real part of the impedance) represents the resistance in series (R_s), which is the combination of the material resistance (current collector, electrode material, electrolyte and separator) and the contact resistance at the electrode/current collector interface. From the high frequency insert in Fig. 8a, we can see that the prolonged CO₂ activation significantly lowered the R_s of the samples. ACM-6h has the lowest R_s value of 0.46 Ω cm², compared with the other activated carbon microspheres and the commercial activated carbon TF-B520. Since the current collector, electrolyte and separator resistances are electrode independent, the CO₂ activation probably only decreases the direct current resistance of the carbon electrodes. Therefore, the decreased R_s is mainly caused by the reducing of the contact resistance at the electrode/current collector

interface upon the carbon activation [52]. R_{CT} , as reflected by the semicircle in the high-frequency region, is the charge-transfer resistance at the interface between electrode and electrolyte. ACM-6h shows the smallest semicircle (R_{CT}), indicating that the prolonged CO₂ activation decreases the contact resistance to adsorption/desorption of ions on carbon electrode. Another important parameter in the Nyquist plot is the Warburg resistance (Z_w), which characterizes the ion diffusion/transport process from the electrolyte into the carbon pores. Z_w can be obtained by the projected length of Warburg-type line (the 45° slope line in the medium-frequency region) onto the X-axis. C_L is the capacitance limit [44,53,54]. Among all the samples, ACM-2h shows apparently higher Z_w , the increased value indicates an increased resistance faced by the electrolyte ions during their transport into the micropores. With increasing activation time, Z_w decreases dramatically, being in accordance with the results of the CV measurements. As expected, a longer activation time evidently lowers the porosity contribution to the total resistance, due to the widening of the pore channels and the reducing of the narrow bottle-neck portions in the micropores.

The capacitance frequency responses of the activated carbon microspheres calculated from EIS are presented in Fig. 8b. Comparing the frequencies at which capacitance drops to half of its maximum value ($C/C_{max} = 0.5$), one clearly see that ACM-6h demonstrates the fastest frequency response with a frequency value of 4.6 Hz. This value is an order of magnitude higher than that of the commercial activated carbon TF-B520 for supercapacitors (0.46 Hz, Fig. 8b), and the other reported activated carbons in aqueous electrolytes [28–40,52,55]. It even exceeds that of advanced activated carbon film (0.9 Hz) with thickness of only 1–2 μm without adding electrically isolative polymer binder in the electrodes [56], and approaches that of zeolite Y-templated carbons with aligned pore channels for ultra-fast power storage and delivery applications [8]. This great frequency response for the sample ACM-6h must be related to the pore widening combined with the elimination of bottle-neck pores. More importantly, the intriguing structure of the activated carbon microspheres provides better penetration of electrolyte and reduces the obstacles for ion diffusion at the electrode material/electrolyte interface.

The performance of EDLCs in real applications is primarily determined by their charge–discharge characteristics, which reveal their energy and power performances. The galvanostatic charge–discharge (C–D) tests under different current densities were performed on the sample ACM-6h, the results are shown in Fig. 9a. The shapes of the C–D curves at all the current densities from 0.5 to 10 A g⁻¹ are linear with no notable IR-drop. Fig. 9b summarizes the effect of increasing current loads (from 0.1 A g⁻¹ to 20 A g⁻¹) in C–D tests on the specific capacitances of the samples ACM-6h and TF-B520. Compared with TF-B520 which is optimized for use in high-power supercapacitor applications, the ACM-6h electrodes show a higher specific capacitance value and a better capacitance retention with a moderate decrease in capacitance from 244 F g⁻¹ to 203 F g⁻¹ (83% retention), even when the current density increases to an ultrahigh value of 20 A g⁻¹. The observed decrease of capacitance at higher currents is generally attributed to the resistance of electrolyte ions traveling in the nanopores and interacting with carbon defects revealed by the high ratio of I_D/I_G in the Raman spectra (Fig. 3). Even though the microspheres of activated carbon have a large volume of micropores, the obtained results are superior to that of various high-capacitance mesoporous carbons. For example, mesoporous carbon synthesized by direct carbonization of citrate salts exhibited specific capacitance of 243 F g⁻¹ at low current density of 0.1 A g⁻¹ in 1 M H₂SO₄ electrolyte, however, it dropped to less than 150 F g⁻¹ at high current density of 20 A g⁻¹ [57]. Mesoporous activated carbon spheres

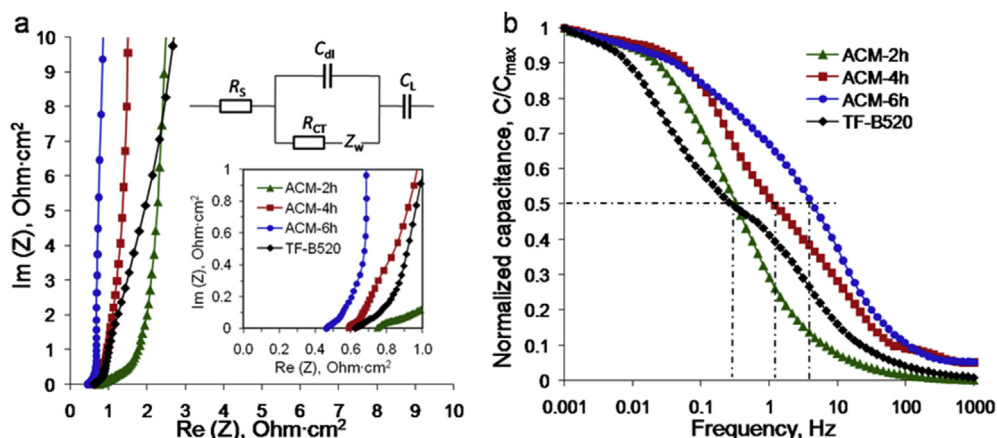


Fig. 8. (a) Nyquist plots and (b) capacitance frequency responses of activated carbon microspheres activated at different activation hours, in comparison with that of commercial activated carbon TF-B520. The top right insert in Fig. 8a is the electrical equivalent circuit and the bottom right insert shows the magnified high frequency region of the plots.

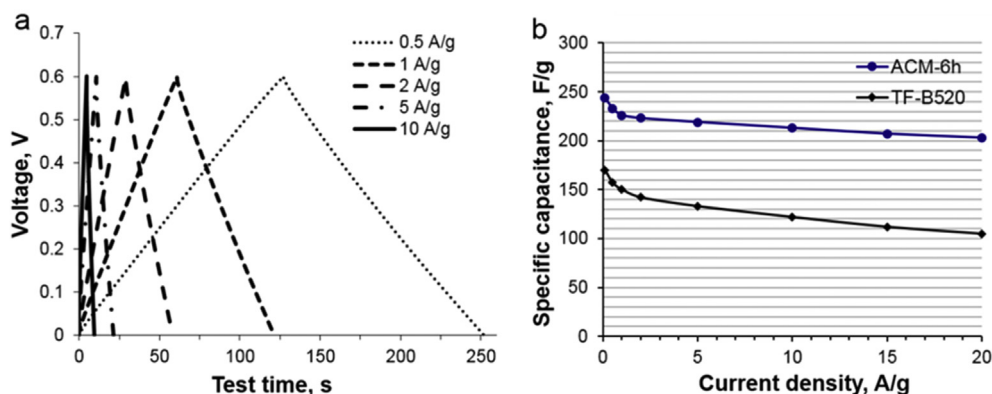


Fig. 9. (a) Galvanostatic charge–discharge curves of symmetric ACM-6h electrode cells in 1 M H_2SO_4 electrolyte under different current densities, and (b) capacitances as a function of current density of ACM-6h electrodes for current densities up to 20 A g^{-1} , with commercial activated carbon TF-B520 for comparison.

derived by the activation of resorcinol-formaldehyde resin presented maximum specific capacitance of 204 F g^{-1} at current density of 0.5 A g^{-1} in 2 M KOH electrolyte, but reduced to 126 F g^{-1} at 20 A g^{-1} [58]. Exfoliated carbon nanosheets from biomass waste corn cob demonstrated a capacitance of 221 F g^{-1} at a 0.5 A g^{-1} rate in 0.5 M H_2SO_4 electrolyte, yet decreased to $\sim 180 \text{ F g}^{-1}$ at 20 A g^{-1} [59]. N-doped mesoporous carbon capsules synthesized by silica-template method offered a specific capacitance of $\sim 240 \text{ F g}^{-1}$ at 0.1 A g^{-1} in 1 M H_2SO_4 electrolyte due to the pseudocapacitive contribution of the N-groups, but the capacitance also fell to $\sim 180 \text{ F g}^{-1}$ at 20 A g^{-1} [60]. The excellent rate capability of the sample ACM-6h is in accordance with the results of CV and EIS measurements. The above findings suggest that the presence of a large portion of mesopores in carbon electrodes is not necessary for getting rapid ion transport, excellent capacity retention and high power characteristics. Though with a large fraction of micropores ($< 2 \text{ nm}$), the hollow microspheres of activated carbon can also provide superior electrochemical performances.

The charge–discharge cycling test was also carried out on the sample ACM-6h at a current density of 2 A g^{-1} , which represents a current density for high-power applications. After 10,000 charge–discharge cycles, the CV curve of ACM-6h retains the rectangular shape (Fig. 10), and exhibits $\sim 4\%$ increasing in the specific capacitance, indicating outstanding cycle stability. The slight increase in the specific capacitance after 10,000 charge–discharge cycles maybe due to the enhanced wettability of the activated carbon microspheres during the charge–discharge process,

therefore some very small micropores become accessible to the electrolyte ions.

4. Conclusions

The biological self-template method, combined with CO_2 activation, is a facile and effective route for converting pollens into

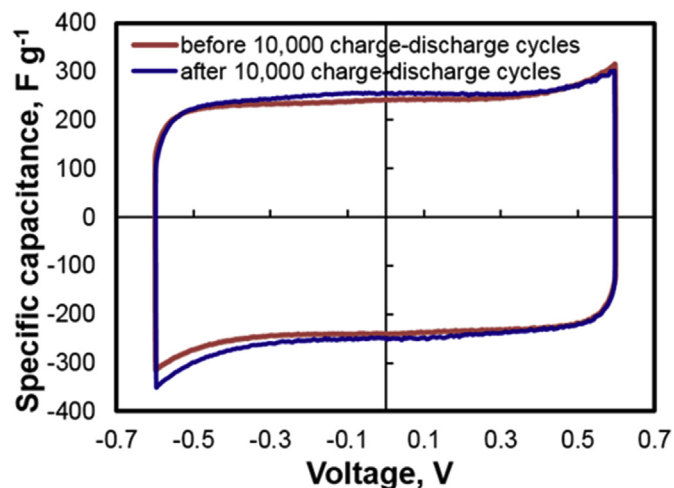


Fig. 10. Cyclic voltammograms of sample ACM-6h at scan rate of 1 mV s^{-1} , before and after 10,000 charge–discharge cycles at current density of 2 A g^{-1} .

activated carbon materials with high surface area, which almost perfectly preserves the intrinsic morphology and structure of pollens as porous hollow microspheres with 3D nanorod network constructed walls. By controlling the CO₂ activation conditions, the specific surface area and pore size distribution of the activated carbon microspheres can be optimized for EDLC applications. Compared with activated carbons used in commercial supercapacitors, our samples, owing to their unique structure, exhibit a great enhancement in the specific capacitance (244 F g⁻¹, ~45% larger than TF-B520 optimized for use in high-power supercapacitor applications), thus offer higher energy density. Furthermore, the activated carbon microspheres present superior rate performance (4 times of TF-B520 at a super-high scan rate of 500 mV s⁻¹), remarkable frequency response (over the other reported activated carbon materials) and excellent charge–discharge cycling stability (no dropping after 10,000 charge–discharge cycles). The above results demonstrate that the microspheres of activated carbon are very promising for high-performance EDLC applications.

Acknowledgments

This work was supported by the National Natural Science Foundation of China (51502105) and the Independent Innovation Foundation of Huazhong University of Science and Technology (2014TS026).

References

- [1] B.E. Conway, *Electrochemical Supercapacitors: Scientific Fundamentals and Technological Applications*, Kluwer-Plenum, New York, 1999.
- [2] A.S. Arico, P. Bruce, B. Scrosati, J.M. Tarascon, W.V. Schalkwijk, *Nat. Mater.* 4 (2005) 366–377.
- [3] J.R. Miller, P. Simon, *Science* 321 (2008) 651–652.
- [4] P. Simon, Y. Gogotsi, *Nat. Mater.* 7 (2008) 845–854.
- [5] E. Frackowiak, F. Beguin, *Carbon* 39 (2001) 937–950.
- [6] L. Wei, G. Yushin, *Nano Energy* 1 (2012) 552–565.
- [7] E. Raymundo-Pinero, K. Kierzek, J. Machnikowski, F. Beguin, *Carbon* 44 (2006) 2498–2507.
- [8] A. Kajdos, A. Kvit, F. Jones, J. Jagiello, G. Yushin, *J. Am. Chem. Soc.* 132 (2010) 3252–3253.
- [9] K. Kim, M. Choi, R. Ryoo, *Carbon* 60 (2013) 175–185.
- [10] J. Chmiola, G. Yushin, Y. Gogotsi, C. Portet, P. Simon, P.L. Taberna, *Science* 313 (2006) 1760–1763.
- [11] Y. Korenblit, M. Rose, E. Kockrick, L. Borchardt, A. Kvit, S. Kaskel, *ACS Nano* 4 (2010) 1337–1344.
- [12] M. Rose, Y. Korenblit, E. Kockrick, L. Borchardt, M. Oschatz, S. Kaskel, G. Yushin, *Small* 7 (2011) 1108–1117.
- [13] H.Y. Jin, Z.H. Peng, W.M. Tang, H.L.W. Chen, *RSC Adv.* 4 (2014) 33022–33028.
- [14] E. Frackowiak, F. Beguin, *Carbon* 40 (2002) 1775–1787.
- [15] G. Lota, K. Fic, E. Frackowiak, *Energy Environ. Sci.* 4 (2011) 1592–1605.
- [16] H. Zhang, G. Gao, Y. Yang, *Energy Environ. Sci.* 2 (2009) 932–943.
- [17] C. Portet, G. Yushin, Y. Gogotsi, *Carbon* 45 (2007) 2511–2518.
- [18] D. Pech, M. Brunet, H. Durou, P.H. Huang, V. Mochalin, Y. Gogotsi, P.L. Taberna, P. Simon, *Nat. Nanotech.* 5 (2010) 651–654.
- [19] Y.J. Lee, J.C. Jung, J. Yi, S.H. Baek, J.R. Yoon, I.K. Song, *Curr. Appl. Phys.* 10 (2010) 682–686.
- [20] B.B. Garcia, S.L. Candelaria, D.W. Liu, S. Sepheri, J.A. Cruz, G.Z. Cao, *Renew. Energy* 36 (2011) 1788–1794.
- [21] B. Xu, S.F. Yue, Z.Y. Sui, X.T. Zhang, S.S. Hou, G.P. Cao, Y.S. Yang, *Energy Environ. Sci.* 4 (2011) 2826–2830.
- [22] Y. Sun, Q. Wu, G. Shi, *Energy Environ. Sci.* 4 (2011) 1113–1132.
- [23] M. Pumera, *Energy Environ. Sci.* 4 (2011) 668–674.
- [24] Y.Y. Peng, Y.M. Liu, J.K. Chang, C.H. Wu, M.D. Ger, N.W. Pu, C.L. Chang, *Carbon* 81 (2015) 347–356.
- [25] J.R. Miller, R.A. Outlaw, B.C. Holloway, *Science* 329 (2010) 1637–1639.
- [26] Y.W. Zhu, S. Murali, M.D. Stoller, K.J. Ganesh, W.W. Cai, P.J. Ferreira, A. Pirkle, R.M. Wallace, K.A. Cychosz, M. Thommes, D. Su, E.A. Stach, R.S. Rouff, *Science* 332 (2011) 1537–1541.
- [27] C. Zheng, X.F. Zhou, H.L. Cao, G.H. Wang, Z.P. Liu, *J. Mater. Chem. A* 3 (2015) 9543–9549.
- [28] W.M. Qiao, Y. Korai, I. Mochida, Y. Hori, T. Maeda, *Carbon* 40 (2002) 351–358.
- [29] L. Wei, M. Sevilla, A.B. Fuertes, R. Mokaya, G. Yushin, *Adv. Energy Mater.* 1 (2011) 356–361.
- [30] B. Xu, Y.F. Chen, G. Wei, G.P. Gao, H. Zhang, Y.S. Yang, *Mater. Chem. Phys.* 124 (2010) 504–509.
- [31] M. Olivares-Marin, J.A. Fernandez, M.J. Lazaro, C. Fernandez-Gonzalez, A. Macias-Garcia, V. Gomez-Serrano, F. Stoeckli, T.A. Centeno, *Mater. Chem. Phys.* 114 (2009) 323–327.
- [32] Y. Gao, L. Li, Y. Jin, Y. Wang, C. Yuan, Y. Wei, G. Chen, J. Ge, H. Lu, *Appl. Energy* 153 (2015) 41–47.
- [33] X.A. Li, W. Xing, S.P. Zhuo, J. Zhou, F. Li, S.Z. Qiao, G.Q. Lu, *Bioresour. Technol.* 102 (2011) 1118–1123.
- [34] V. Subramanian, C. Luo, A.M. Stephan, K.S. Nahm, S. Thomas, B. Wei, *J. Phys. Chem. C* 111 (2007) 7527–7531.
- [35] S. Zhao, C.Y. Wang, M.M. Chen, J. Wang, Z.Q. Shi, *J. Phys. Chem. Solids* 70 (2009) 1256–1260.
- [36] Q.P. Luo, L. Huang, X. Gao, Y. Cheng, B. Yao, Z. Hu, J. Wan, X. Xiao, J. Zhou, *Nanotechnology* 26 (2015) 304004–304010.
- [37] S.G. Lee, K.H. Park, W.G. Shim, M.S. Balathanigaimani, H. Moon, *J. Ind. Eng. Chem.* 17 (2011) 450–454.
- [38] M.S. Balathanigaimani, W.G. Shim, M.J. Lee, C. Kim, J.W. Lee, H. Moon, *Electrochem. Commun.* 10 (2008) 868–871.
- [39] T.E. Rufford, D. Hulicova-Jurcakova, K. Khosla, Z.H. Zhu, G.Q. Lu, *J. Power Sources* 195 (2010) 912–918.
- [40] T.E. Rufford, D. Hulicova-Jurcakova, Z.H. Zhu, G.Q. Lu, *Electrochem. Commun.* 10 (2008) 1594–1597.
- [41] X. Li, C. Han, X. Chen, C. Shi, *Micropor. Mesopor. Mat.* 131 (2010) 303–309.
- [42] L. Zhang, F. Zhang, X. Yang, K. Leng, Y. Huang, Y.S. Chen, *Small* 9 (2013) 1342–1347.
- [43] L. Wei, G. Yushin, *J. Power Sources* 196 (2011) 4072–4079.
- [44] H. Li, B. Wang, X. He, J. Xiao, H. Zhang, Q. Liu, J. Liu, J. Wang, L. Liu, P. Wang, *J. Mater. Chem. A* 3 (2015) 9754–9762.
- [45] Y. Wang, Z. Liu, B. Han, Y. Huang, G. Yang, *Langmuir* 21 (2005) 10846–10849.
- [46] L. Wei, M. Sevilla, A.B. Fuertes, R. Mokaya, G. Yushin, *Adv. Funct. Mater.* 22 (2012) 827–834.
- [47] G.N. Yushin, E.N. Hoffman, A. Nikitin, H. Ye, M.W. Barsoum, Y. Gogotsi, *Carbon* 44 (2005) 2075–2082.
- [48] P.H. Tan, S. Dimovski, Y. Gogotsi, *Phil. Trans. R. Soc. Lond. A* 362 (2004) 2289–2310.
- [49] R.T. Yang, *Adsorbents: Fundamentals and Applications*, John Wiley & Sons, Hoboken, NJ, 2003.
- [50] O. Barbieri, M. Hahn, A. Herzog, R. Kotz, *Carbon* 43 (2005) 1303–1310.
- [51] P.L. Taberna, P. Simon, J.F. Fauvarque, *J. Electrochem. Soc.* 150 (2003) A292–A300.
- [52] L. Wei, G. Yushin, *Carbon* 49 (2011) 4830–4838.
- [53] Z. Fan, J. Yan, T. Wei, L. Zhi, G. Ning, T. Li, F. Wei, *Adv. Funct. Mater.* 21 (2011) 2366–2375.
- [54] A. Di Fabio, A. Giorgi, M. Mastragostino, F. Soavi, *J. Electrochem. Soc.* 148 (2001) A845–A850.
- [55] W. Gu, M. Sevilla, A. Magasinski, A.B. Fuertes, G. Yushin, *Energy Environ. Sci.* 6 (2013) 2465–2476.
- [56] L. Wei, N. Nitta, G. Yushin, *ACS Nano* 7 (2013) 6498–6506.
- [57] G.A. Ferrero, M. Sevilla, A.B. Fuertes, *Carbon* 88 (2015) 239.
- [58] Y. Wang, B. Chang, D. Guan, X. Dong, *J. Solid State Electr.* 6 (2015) 1783–1791.
- [59] M. Genovese, J. Jiang, K. Lian, N. Holm, *J. Mater. Chem. A* 3 (2015) 2903–2913.
- [60] G.A. Ferrero, A.B. Fuertes, M. Sevilla, *J. Mater. Chem. A* 3 (2015) 2914–2923.